Chen *et al. Chem. Synth.* **2025**, *5*, 51
DOI: 10.20517/cs.2024.156

Chemical Synthesis

Research Article

Open Access

Check for updates

Ce(IV)-MOF supported bimetallic NiPt nanoparticles for efficient hydrogen generation from ammonia borane hydrolysis

Xinshun Chen[1], Siyu Hao[1], Jiapei Wang[1,*], Lixin Xu[1,*], Shenglai Li[2], Chao Wan[1,3,4,*], Pavel S. Postnikov[5]

[1]School of Chemistry and Chemical Engineering, Anhui University of Technology, Ma'anshan 243002, Anhui, China.
[2]Department of Materials Science and Chemical Engineering, Stony Brook University, New York, NY 11794, USA.
[3]Shaoxing Research Institute Renewable Energy and Molecular Engineering, Shanghai Jiao Tong University, Shaoxing 312300, Zhejiang, China.
[4]Key Laboratory of Advanced Energy Materials Chemistry, Ministry of Education, Nankai University, Tianjin 300071, China.
[5]Research School of Chemistry and Applied Biomedical Sciences, Tomsk Polytechnic University, Tomsk 6340034, Russian Federation.

[*]**Correspondence to:** Jiapei Wang, Prof. Lixin Xu, Dr. Chao Wan, School of Chemistry and Chemical Engineering, Anhui University of Technology, No. 1530 Maxiang Rd, Ma'anshan 243002, Anhui, China. E-mail: jpwang@ahut.edu.cn; lxxu@hotmail.com; wanchao1219@hotmail.com

How to cite this article: Chen, X.; Hao, S.; Wang, J.; Xu, L.; Li, S.; Wan, C.; Postnikov, P. S. Ce(IV)-MOF supported bimetallic NiPt nanoparticles for efficient hydrogen generation from ammonia borane hydrolysis. *Chem. Synth.* **2025**, *5*, 51. https://dx.doi.org/10.20517/cs.2024.156

Received: 1 Nov 2024 **First Decision:** 3 Jan 2025 **Revised:** 14 Feb 2025 **Accepted:** 21 Feb 2025 **Published:** 20 May 2025

Academic Editor: Guangshan Zhu **Copy Editor:** Pei-Yun Wang **Production Editor:** Pei-Yun Wang

Abstract

Supported bimetallic catalysts exhibit excellent catalytic activity in the hydrogen generation reaction for hydrogen storage materials, where the synergism interaction between the support and the metal needs to be explored. In this work, highly crystalline cerium-based metal-organic framework (CeMOF) supports were prepared to support NiPt alloy nanoparticles for the ammonia borane (AB) hydrolysis. CeMOF supports not only possess stable structural properties and low synthesis costs, but also provide more active sites to facilitate AB hydrolysis. The optimal catalyst, $Ni_{0.6}Pt_{0.4}$/CeMOF, exhibits a significant turnover frequency (11.07 mol_{H2}·mol_{Pt}·min^{-1}) at 298 K, with the conversion of AB reaching 100%. This work contributes a new, cost-effective approach for designing efficient catalysts that can be used in hydrogen generation systems, which is important for the development of sustainable energy storage technologies.

Keywords: Ammonia borane, hydrogen production, CeMOF, NiPt alloy nanoparticles

INTRODUCTION

The escalating energy crisis has prompted the search for efficient and sustainable renewable energy sources to replace traditional fossil fuels. Among these, hydrogen is a promising new energy carrier. One kilogram of hydrogen releases 142,351 kJ of heat when burned, and its combustion products are clean and pollution-free[1-4]. However, the safe production and transportation of hydrogen gas remain significant challenges[5,6]. Ammonia borane (AB) hydrolysis has emerged as a highly promising method for producing green hydrogen, helping to reduce carbon dioxide emissions. AB has a hydrogen storage density of up to 19.6 wt%, and it demonstrates considerable stability in water[7-11]. In the presence of an appropriate catalyst, 1 mol of AB can release 3 mol of hydrogen gas through hydrolysis[12-14]:

$$(NH_3BH_3 + 2H_2O = NH_4^+ + BO_2^- + 3H_2) \quad (1)$$

However, the catalytic performance of most catalysts is significantly diminished at low temperatures. Therefore, developing a catalyst that can efficiently catalyze AB hydrolysis and release hydrogen gas under mild conditions remains a major challenge. Among these, single-metal catalysts based on Co[15,16], Rh[17], Pt[18-20], Cu[21] exhibit excellent catalytic activity for AB hydrolysis. In particular, heterogeneous catalysts with Pt nanoparticles (NPs) dispersed on various supports show outstanding activity[22-24]. The combination of numerous metal and organic ligands allows for flexible regulation of the electronic state of the metal component, offering potential advantages over other individual porous solids. This enables the design of catalysts with tailored structures and compositions to meet specific requirements.

Although precious metal-based catalysts typically exhibit high catalytic activity, their susceptibility to high-temperature sintering can negatively affect their performance. Non-precious metal catalysts, while generally exhibiting lower catalytic activity, are more cost-effective and often demonstrate excellent activity and thermal stability. Bimetallic nanocatalysts combining precious and non-precious metals, such as PtFe[25], NiCo[26,27], PtCo[28], and PtNi[29], show significant catalytic activity in the AB hydrolysis reaction. This enhanced performance is attributed to the synergistic effect between two metals, which generates more active sites[30-35]. Additionally, this bimetallic strategy effectively reduces the cost of the catalyst. Therefore, the development of bimetallic nanocatalysts, particularly those combining precious and non-precious metals, is a promising research direction. Bimetallic nanocatalysts are classified into ordered and disordered alloy catalysts, based on the proportion and arrangement of metal components. These catalysts offer high efficiency and selectivity and are widely applicable in various catalytic processes. Common methods for bimetal loading on supports include hydrogen reduction, immersion reduction, and photocatalytic reduction. Recent research on alloy nanocatalysts for AB hydrolysis has yielded exciting results. For example, Li *et al.* discovered a high-performance PtCo alloy supported on polyethylene imine-modified graphene oxide catalyst for AB hydrolysis[28]. Wang *et al.* synthesized Pt-M (M = Fe, Co, Ni) bimetallic NPs in aqueous solution for catalyzing AB hydrolysis[29]. Yang *et al.* developed an effective Ni-Fe-P/NF ternary catalyst for AB hydrolysis[36]. However, the high cost of nickel-platinum catalysts produced by these methods makes them unsuitable for large-scale production.

Previous research has shown that, in addition to Pt-based materials, Ni-based catalysts also exhibit activity in AB hydrolysis reactions[29]. Currently, there are several examples of NiPt bimetallic catalysts for hydrogen production from hydrazine hydrate[37-39], but the application of catalyzing AB hydrolysis is relatively rare. For example, the addition of a small amount of Pt to Ni/Al_2O_3 significantly enhances the activity and stability of the catalyst, as the close contact between Ni and Pt increases the dispersion of the Ni metal[40,41]. Tetravalent cerium-based metal-organic frameworks (CeMOF) exhibit highly stable chemical properties due to the strong coordination bonds in their internal structure[42-45]. Based on the high stability, low

synthesis cost, and high redox activity of tetravalent CeMOF, the catalytic performance of NiPt/CeMOF alloy catalysts in AB hydrolysis reactions was investigated. CeMOF was synthesized using terephthalic acid and cerium ammonium nitrate as raw materials in a mixed solvent of acetic acid, ethanol, and water under 308 K. A series of NiPt/CeMOF catalysts with controllable NiPt composition were then prepared using an impregnation reduction method. The results showed that the optimal catalyst, $Ni_{0.6}Pt_{0.4}$/CeMOF, exhibited a significant turnover frequency (TOF; 11.07 $mol_{H_2}·mol_{Pt}·min^{-1}$) and an activation energy of 54.04 ± 2.35 $kJ·mol^{-1}$ under 298 K, and it also showed excellent stability and recyclability. Finally, the catalyst was characterized by X-ray diffraction (XRD), X-ray photoelectron spectroscopy (XPS), transmission electron microscopy (TEM), scanning electron microscopy (SEM), and Fourier transform infrared (FTIR) spectroscopy techniques, and the effects of various reaction temperatures, catalyst dosages, and other conditions on the catalyst performance were also studied.

EXPERIMENTAL

Material

Cerium ammonium nitrate [$Ce(NH_4)_2(NO_3)_6$, AR], terephthalic acid ($C_8H_6O_4$, 99%), and AB (NH_3BH_3, 97%) were purchased from Shanghai Aladdin Biochemical Technology Co., Ltd. Nickel chloride hexahydrate ($NiCl_2·6H_2O$, AR), sodium hydroxide (NaOH, AR), acetic acid (CH_3COOH, AR), and anhydrous ethanol (C_2H_6O, AR) were purchased from Sinopharm Chemical Reagent Co., Ltd. Chloroplatinic acid ($H_2PtCl_6·6H_2O$ AR) was purchased from Nanjing Chemical Reagent Co., Ltd. Sodium borohydride ($NaBH_4$ 98%) was purchased from Shanghai Adamas Co., Ltd.

Preparation of CeMOF support

First, 820 mg of cerium ammonium nitrate, 3 mL of acetic acid, 8 mL of distilled water, and 20 mL of ethanol were mixed in a beaker and stirred at 35 °C until the cerium ammonium nitrate dissolved completely. Subsequently, 249 mg of terephthalic acid was added to the above-mentioned solution, and the mixture was stirred for 1.5 h before being cooled to room temperature. The resulting precipitate was separated by centrifugation, washed alternately with water and ethanol three times, and dried in an oven at 338 K. Finally, the obtained milky-yellow powder is the CeMOF support.

Preparation of NiPt/CeMOF catalyst

The NiPt/CeMOF catalyst was synthesized by a simple one-step co-reduction method, using CeMOF as the support and $NaBH_4$ as a reducing agent at room temperature. Taking the $Ni_{0.6}Pt_{0.4}$/CeMOF catalyst as an example, the specific steps are illustrated in Figure 1. A solution containing $NiCl_2·6H_2O$ and $H_2PtCl_6·6H_2O$ in a metal molar ratio of 6:4 was mixed into a beaker, followed by the addition of 0.2 g of CeMOF support, and the mixture was stirred evenly for 24 h. The beaker was put into a low-temperature bath at 270 K. Subsequently, 2 mL of deionized water containing 0.02 g of $NaBH_4$ and 0.04 g of NaOH was added, and the mixture was stirred for over 5 h to accomplish the complete reduction of the metal. The resulting product was centrifuged, dried for 12 h, and ground to obtain the $Ni_{0.6}Pt_{0.4}$/CeMOF catalyst. Using the same method, NiPt/CeMOF catalysts with different molar ratios of 1:0, 2:8, 3:7, 4:6, 8:2, 9:1, and 0:1 were prepared and named Ni/CeMOF, $Ni_{0.2}Pt_{0.8}$/CeMOF, $Ni_{0.3}Pt_{0.7}$/CeMOF, $Ni_{0.4}Pt_{0.6}$/CeMOF, $Ni_{0.8}Pt_{0.2}$/CeMOF, $Ni_{0.9}Pt_{0.1}$/CeMOF, and Pt/CeMOF, respectively. The total amount of NiPt metal used in all cases was 0.05 mmol.

Characterization

TEM images were acquired using a JEM-2000FX transmission electron microscope (JEOL Corporation, Japan), operating at 200 kV. The XRD patterns of the samples were recorded using a Bruker AXS D8 Advance X-ray diffractometer, equipped with a copper target (Cu Ka, λ = 1.54056) as the diffraction source, operating at an acceleration voltage of 40.0 kV, with a scanning range of 2θ = 10°-80°. SEM images were obtained using a Zeiss Gemini 300 field-emission scanning electron microscope. The surface elemental

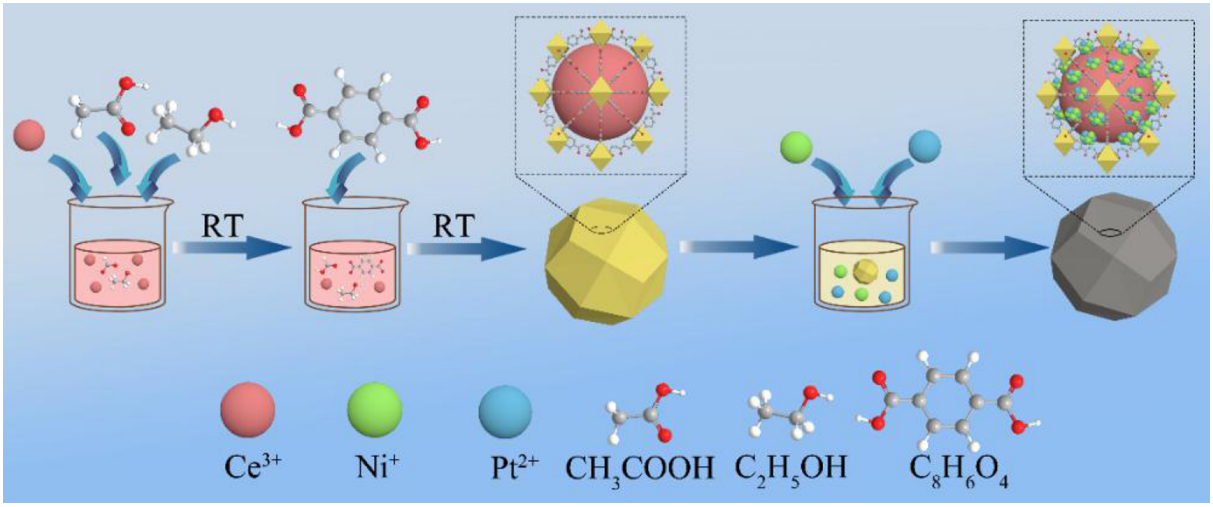

Figure 1. Schematic diagram of NiPt/CeMOF catalyst synthesis. CeMOF: Cerium-based metal-organic framework.

composition and chemical state of the sample were analyzed using Thermo Scientific K-Alpha XPS. The framework structure of the CeMOF support was characterized by FTIR spectroscopy.

AB hydrolysis reaction over NiPt/CeMOF catalyst

The catalytic performance of NiPt/CeMOF catalyst was evaluated by measuring the hydrogen production from AB hydrolysis using water displacement method. In this setup, 0.02 g of catalyst was placed into a double-necked jacketed reaction flask. The reaction temperature was controlled by a low-temperature water bath. Once the temperature stabilized at 298 K, 2 mL of deionized water containing 1 mmol AB was injected into the reaction flask. Timing was initiated upon the appearance of the first bubble, and the time was recorded at each 5 mL drop in water level until the reaction was complete, as indicated by a stable liquid level. The TOF of the NiPt/CeMOF catalyst was calculated using

$$TOF = n(H_2)/[n(metal)\ t] \quad (2)$$

where $n(H_2)$ represents the molar amount of H_2 released at a 20% conversion of AB, n(metal) represents the total molar amount of metal atoms in the catalyst, and t is the time consumed when the reaction conversion reaches 20%.

Stability of NiPt/CeMOF catalyst for AB hydrolysis

The stability of the NiPt/CeMOF catalyst in AB hydrolysis reaction was assessed by evaluating its reusability at room temperature. The specific procedure for the cyclic stability test is as follows: In the first test reaction, 20 mg of NiPt/CeMOF catalyst was used for the hydrolysis reaction of AB. Upon completion of the reaction, the reaction mixture was centrifuged, and the catalyst was washed with ethanol to remove surface residues. The recovered catalyst was then dried for reuse. Subsequently, the recovered catalyst was subjected to a second reaction under the same conditions as the first reaction, and the reaction data were recorded. This process was repeated five times under identical conditions to investigate the reusability of the catalyst.

RESULTS AND DISCUSSION

A suitable amount of CeMOF support was put into a mixed solution of $NiCl_2·6H_2O$ and $H_2PtCl_6·6H_2O$, followed by the addition of $NaBH_4$ and NaOH used as reducing agents, to synthesize monodisperse NiPt NPs on the surface of the CeMOF support. Seven different compositions of NiPt NPs were synthesized, including Ni/CeMOF, $Ni_{0.2}Pt_{0.8}$/CeMOF, $Ni_{0.3}Pt_{0.7}$/CeMOF, $Ni_{0.6}Pt_{0.4}$/CeMOF, $Ni_{0.8}Pt_{0.2}$/CeMOF, $Ni_{0.9}Pt_{0.1}$/CeMOF, and Pt/CeMOF. The CeMOF support, Ni/CeMOF, Pt/CeMOF, and $Ni_{0.6}Pt_{0.4}$/CeMOF catalysts were characterized by SEM. Figure 2A-D reveals that all four samples exhibit irregular particle shapes, and the morphology of the CeMOF support remains unchanged after metal loading, indicating that the CeMOF support possesses good structural stability. TEM was further employed to characterize $Ni_{0.6}Pt_{0.4}$/CeMOF and Pt/CeMOF. Figure 3A and B shows that the average particle size distribution of NiPt NPs is 2.65 ± 0.79 nm. It can be found that the fit is approximate as Figure 3B is clearly not Gaussian. Figure 3C and D indicates that Ni and Pt metal particles are uniformly dispersed on the surface of CeMOF without signs of agglomeration. Figure 4A and B reveals characteristic vibration peaks at 1,507 cm^{-1} for the terephthalate ion and 1,380 cm^{-1} for the acetate ion, confirming the successful synthesis of a highly crystalline CeMOF support[43].

The crystal structure of bimetallic NiPt NPs was determined by analyzing the XRD patterns of Ni, Pt, and $Ni_{0.6}Pt_{0.4}$ [Figure 4C and D]. The results indicated that both Pt and NiPt NPs are face-centered cubic (111) lattices. The characteristic peak of monometallic nickel (111) appears at $2\theta = 43.6°$, while the peak of monometallic platinum (111) is observed at $2\theta = 39.5°$. However, due to the high dispersion of the metal on the support surface and the small crystal size, the diffraction intensity is not prominent. The XRD pattern of NiPt/CeMOF reveals that as the Ni content increases, a noticeable rightward shift in the peak position occurs, confirming the successful alloying of Ni and Pt. The peak at $2\theta = 7.1°$ corresponds to the CeMOF structure[43]. After loading the NiPt active metal component, the diffraction peaks of Ni/CeMOF, Pt/CeMOF, and $Ni_{0.6}Pt_{0.4}$/CeMOF samples remain unchanged, demonstrating the structural stability of the CeMOF support.

The surface elemental valence states of the NiPt/CeMOF catalyst were analyzed using XPS. The XPS spectra shown in Figure 5A-F reveal the core peaks of Ni, Pt, Ce, C, and O, confirming the presence of the active NiPt component within the catalyst. The peaks at 529.6 and 531.1 eV in Figure 5C correspond to the spin-splitting coupling of O*1s*, respectively. As illustrated in Figure 5E, the characteristic peaks of Ni $2p_{3/2}$ and Ni $2p_{1/2}$ are observed at 856.35 and 873.84 eV, respectively, while oxidized Ni atoms give rise to additional peaks at 861.97 and 882.54 eV. In the XPS spectrum of the Pt 4*f* energy level [Figure 5F], two main peaks are present at 72.23 and 75.43 eV, representing metallic Pt atoms. The peak at 71.89 eV belongs to the metal Pt NPs, and the NiPt/CeMOF binding energy is shifted to a higher energy state by 0.34 eV [Figure 6A]; In contrast, the peak at 856.76 eV belongs to the metal Ni NP, with the NiPt/CeMOF binding energy shifted to a lower energy state by 0.41 eV [Figure 6B]. These shifts in binding energy further confirm that NiPt NPS in NiPt/CeMOF has an alloy structure.

The catalytic performance of different catalysts was evaluated to investigate the effect of alloy on the catalytic performance. Figure 7A shows the relationship between the volume of hydrogen gas produced by AB hydrolysis and reaction time catalyzed by NiPt/CeMOF catalysts with different NiPt molar ratios at 298 K. Seven different NiPt NP compositions were tested, including Ni/CeMOF, $Ni_{0.2}Pt_{0.8}$/CeMOF, $Ni_{0.3}Pt_{0.7}$/CeMOF, $Ni_{0.6}Pt_{0.4}$/CeMOF, $Ni_{0.8}Pt_{0.2}$/CeMOF, $Ni_{0.9}Pt_{0.1}$/CeMOF, and Pt/CeMOF. The results show that monometallic Ni/CeMOF exhibits no catalytic activity for AB hydrolysis, while Pt/CeMOF demonstrates significant catalytic performance but incurs higher costs. The catalytic performance of alloyed NiPt/CeMOF was significantly enhanced, with the $Ni_{0.6}Pt_{0.4}$/CeMOF catalyst showing the highest activity. Figure 7B

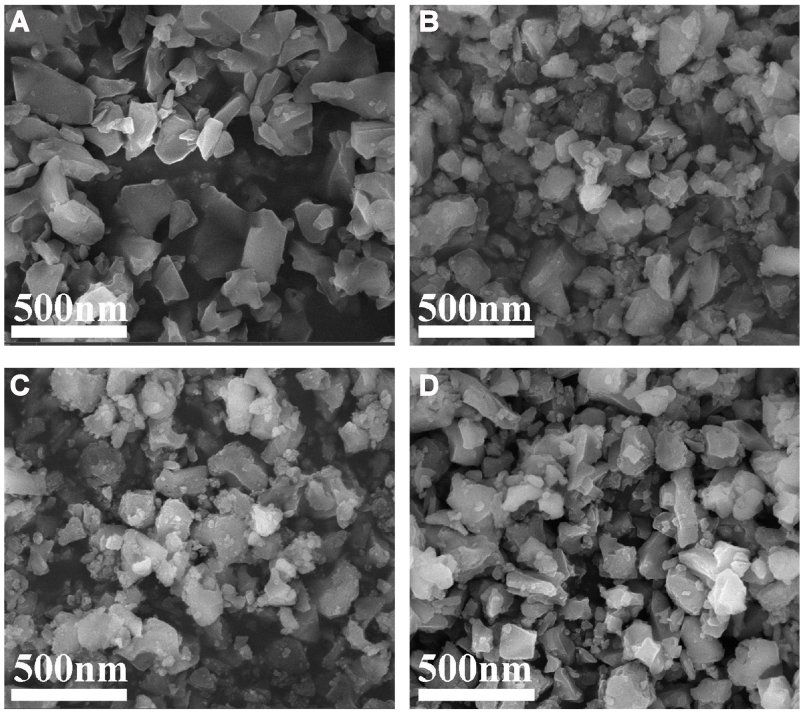

Figure 2. SEM images at the same magnification: (A) CeMOF, (B) Ni/CeMOF, (C) Pt/CeMOF, (D) $Ni_{0.6}Pt_{0.4}$/CeMOF. SEM: Scanning electron microscopy; CeMOF: cerium-based metal-organic framework.

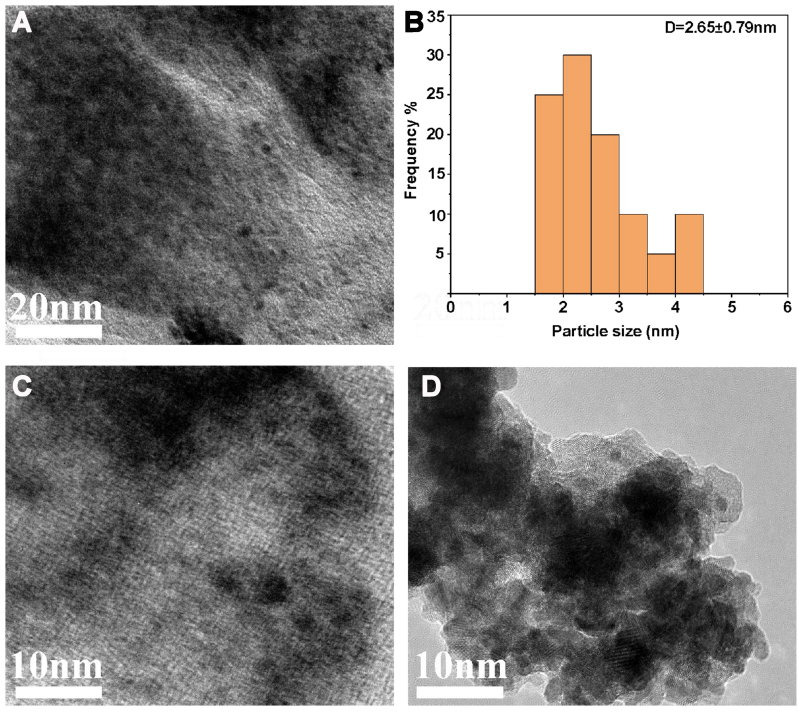

Figure 3. TEM images of NiPt NPs on $Ni_{0.6}Pt_{0.4}$/CeMOF, (A and C) $Ni_{0.6}Pt_{0.4}$, (B) NiPt alloy particle size, (D) Pt. TEM: Transmission electron microscopy; NPs: nanoparticles; CeMOF: cerium-based metal-organic framework.

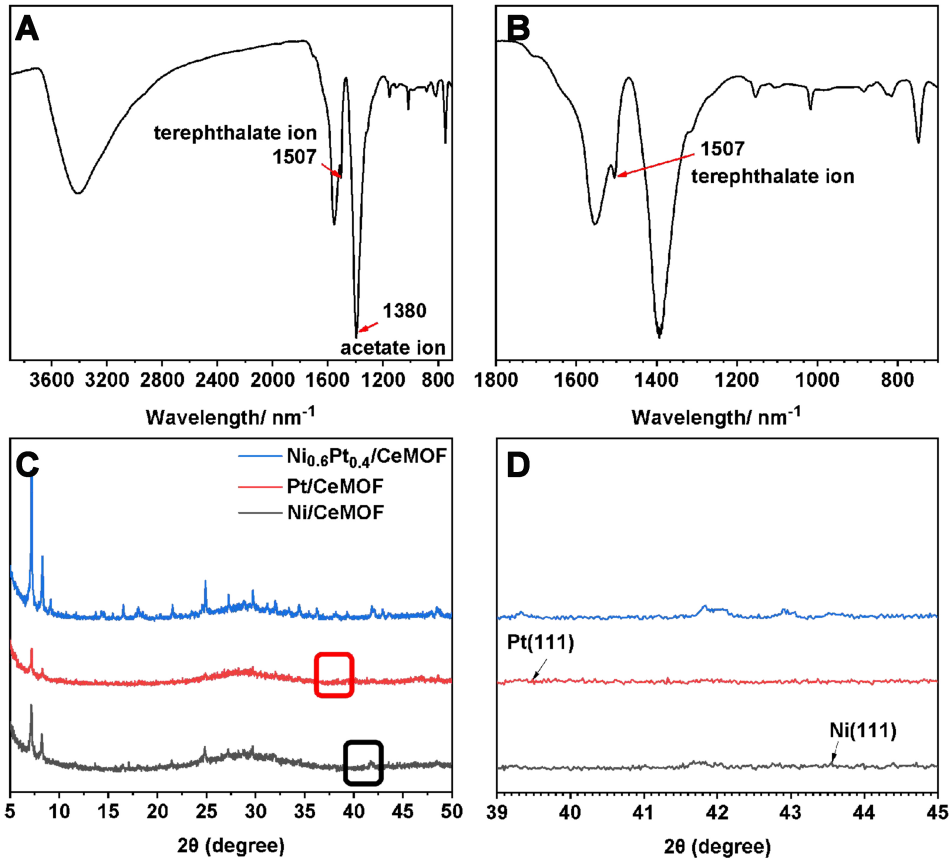

Figure 4. (A and B) Ce (IV)-MOF infrared spectrum; (C and D) XRD patterns of Ni/CeMOF, Pt/CeMOF, and $Ni_{0.6}Pt_{0.4}$/CeMOF. MOF: Metal-organic framework; XRD: X-ray diffraction; CeMOF: cerium-based metal-organic framework.

displays the TOF values for the seven catalysts. At a total metal molar amount of 0.05 mmol, the $Ni_{0.6}Pt_{0.4}$/CeMOF catalyst achieved a maximum TOF value of 11.07 mol_{H_2}·mol_{Pt}·min^{-1}. For example, in the absence of visible light, it takes 16.5 min for AB to be fully catalyzed by the $Ni_{40}Pt_{60}/TiO_2$ catalyst prepared by Wan *et al.*[38]. Increasing or decreasing the Ni content from this ratio resulted in reduced reaction rates, suggesting a synergistic effect between Ni and Pt in the alloy. The effect of $Ni_{0.6}Pt_{0.4}$/CeMOF catalyst dosage and AB concentration on AB hydrolysis was further investigated. Figure 7C shows the hydrogen production volume and reaction time curves for catalyst dosages ranging from 20 to 40 mg at 298 K. The results indicated that the hydrolysis rate increased with higher catalyst dosages. In Figure 7D, the reaction rates of different catalyst concentrations were calculated, and the logarithm of the reaction rate (ln[rate]) was plotted against the logarithm of catalyst concentration (ln[cat]). A linear relationship was observed, confirming that the reaction rate is proportional to the catalyst concentration. The influence of AB concentration on catalytic performance was examined while keeping other parameters constant. Figure 7E depicts the hydrogen gas volume and reaction time for 20 mg of $Ni_{0.6}Pt_{0.4}$/CeMOF catalyst at various AB concentrations. While the hydrogen gas volume increased with higher AB concentrations, the dehydrogenation rate remained constant. The logarithm of the hydrolysis reaction rate (ln[k]) was plotted against the logarithm of AB concentration (ln[AB]), resulting in the linear equation $\ln[k] = 0.066\ln[AB] + 2.54$ with a slope close to zero [Figure 7F]. This indicates that the reaction is zero-order with respect to AB concentration, and the reaction rate is independent of AB concentration in the presence of $Ni_{0.6}Pt_{0.4}$/CeMOF catalyst.

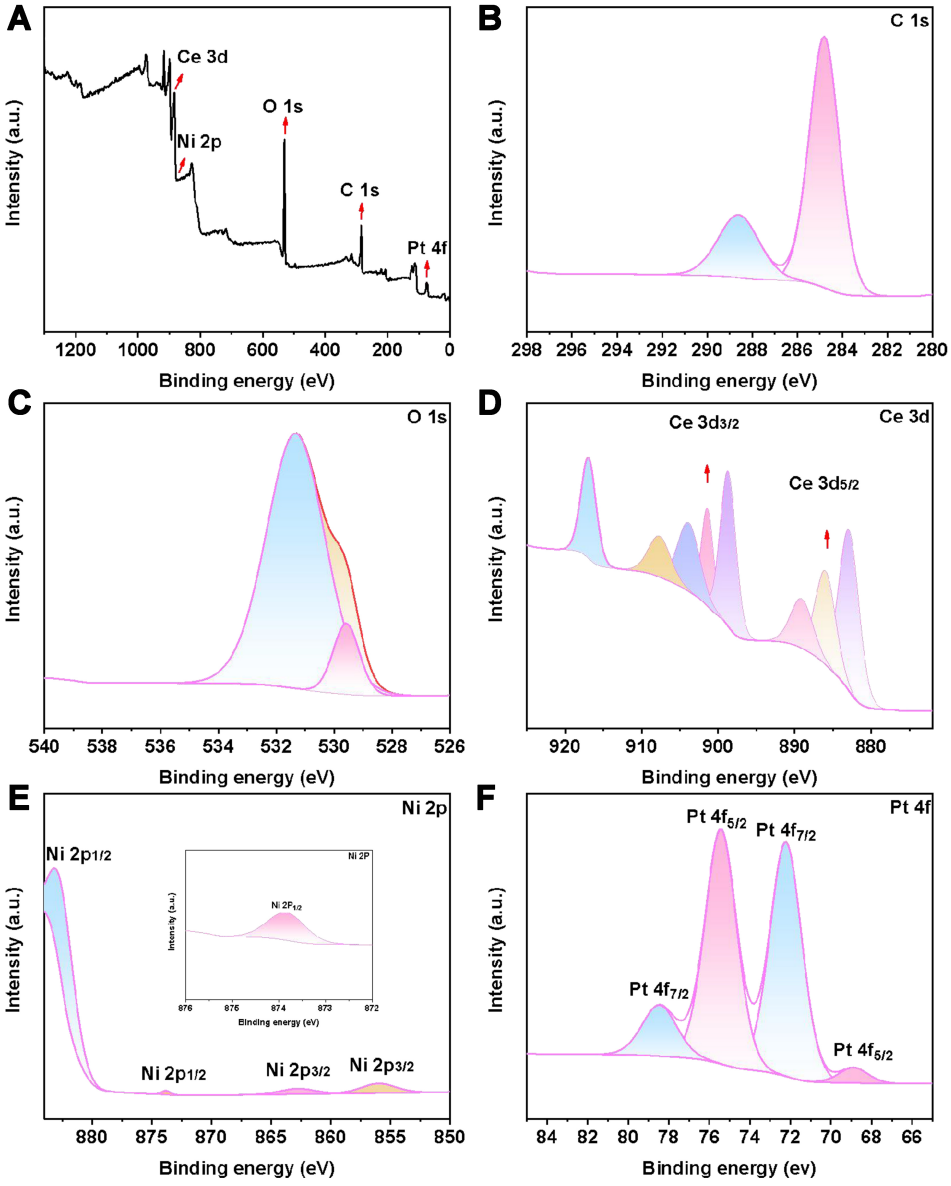

Figure 5. (A) XPS full spectrum of $Ni_{0.6}Pt_{0.4}$/CeMOF, (B) C 1*s*, (C) O 1*s*, (D) Ce 3*d*, (E) Ni 2*p*, (F) Pt 4*f*. XPS: X-ray photoelectron spectroscopy; CeMOF: cerium-based metal-organic framework.

Finally, we investigated the effect of temperature (293-313 K) on AB hydrolysis while maintaining constant AB (1 mmol) and $Ni_{0.6}Pt_{0.4}$/CeMOF (20 mg) dosages. Figure 8A illustrates the relationship between the volume of hydrogen gas produced and reaction time under varying temperature conditions. As expected, the reaction rate increased with temperature, significantly reducing the time required for complete hydrolysis of AB from 7.36 to 1.43 min. The reaction rates were calculated from the reaction curves at different temperatures [Figure 8A], and the corresponding reaction rate constants (k) were determined. Subsequently, the logarithm of k (ln[k]) was plotted against the reciprocal of the reaction temperature (1/T), as shown in Figure 8B. The resulting linear equation was $\ln[k] = 24.30 - (6.5 \pm 0.283)\ (1{,}000/T)$. From this, the activation energy for the AB hydrolysis reaction catalyzed by $Ni_{0.6}Pt_{0.4}$/CeMOF was calculated to be 54.04 ± 2.35 kJ/mol.

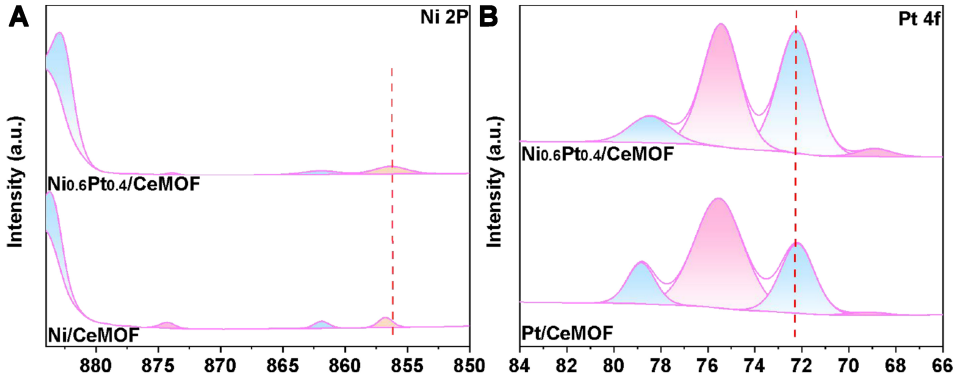

Figure 6. (A) Comparison of XPS spectra of $Ni_{0.6}Pt_{0.4}$/CeMOF and Ni/CeMOF in the Ni 2*P* regions; (B) Comparison of XPS spectra of $Ni_{0.6}Pt_{0.4}$/CeMOF and Pt/CeMOF in the Pt 4*f* regions. XPS: X-ray photoelectron spectroscopy; CeMOF: cerium-based metal-organic framework.

The cyclic stability of $Ni_{0.6}Pt_{0.4}$/CeMOF catalyst in catalyzing AB hydrolysis was evaluated, and Figure 8C shows the relationship between the volume of hydrogen released and the reaction time during each cycle. At 298 K, data from the first AB hydrolysis reaction catalyzed $Ni_{0.6}Pt_{0.4}$/CeMOF were recorded, and the used catalyst was recovered. Four subsequent AB hydrolysis experiments were then conducted under identical reaction conditions, and the corresponding hydrogen volume and reaction time curves were plotted. The results demonstrate that the $Ni_{0.6}Pt_{0.4}$/CeMOF catalyst maintains its catalytic activity over five reaction cycles, as shown in Figure 8C, with further confirmation of its excellent cyclic stability provided by the data in Figure 8D. The increasing reaction time observed for each cycle is attributed to the partial loss of NiPt alloy particles during the reaction, which affects the catalytic activity over successive cycles.

The hydrolysis mechanism of AB over $Ni_{0.6}Pt_{0.4}$/CeMOF involves several key steps. Initially, the $Ni_{0.6}Pt_{0.4}$ alloy NPs, supported on the highly crystalline CeMOF, provide active catalytic sites for the interaction with AB. The process begins with the adsorption of AB onto the catalyst surface, where the strong metal-support interactions facilitate the weakening of the B–H bonds in AB. Subsequently, hydroxyl ions from the aqueous medium attack the boron atom in AB, leading to B–H bond cleavage and the formation of boron oxides and hydrogen gas. The unique electronic properties and geometric structure of the $Ni_{0.6}Pt_{0.4}$ alloy improve the reaction's activation energy by stabilizing transition states, thereby accelerating the reaction rate. As the reaction progresses, the desorption of generated hydrogen molecules from the catalyst surface occurs, while residual species from AB hydrolysis continue to react, resulting in the complete conversion of AB into hydrogen. The catalytic activity of $Ni_{0.6}Pt_{0.4}$/CeMOF is further augmented by the porous structure of the CeMOF support, which provides a larger surface area and an abundance of active sites, promoting efficient hydrogen production. Although the high cost of Pt (132.5 $/g) limits its industrial application, the incorporation of the cheap metal Ni (5.7 $/g) can significantly reduce the overall cost of the catalyst. This is prone to the cost of the NiPt alloy for large-scale applications.

CONCLUSION

In summary, we report a simple impregnation reduction method for preparing a novel catalyst for AB hydrolysis. Firstly, CeMOF was prepared by an oil bath thermal method, followed by the successful preparation of a series of NiPt/CeMOF nanocatalysts for AB hydrolysis. By varying the Ni/Pt molar ratio, the optimal $Ni_{0.6}Pt_{0.4}$/CeMOF exhibited the best catalytic activity, complete hydrogen generation from AB hydrolysis in just 5.6 min at 298 K, with a TOF reaching 11.07 $mol_{H_2} \cdot mol_{Pt} \cdot min^{-1}$, exceeding most of the reported catalysts in literature. Additionally, the catalyst demonstrated excellent stability after 5 cycles of

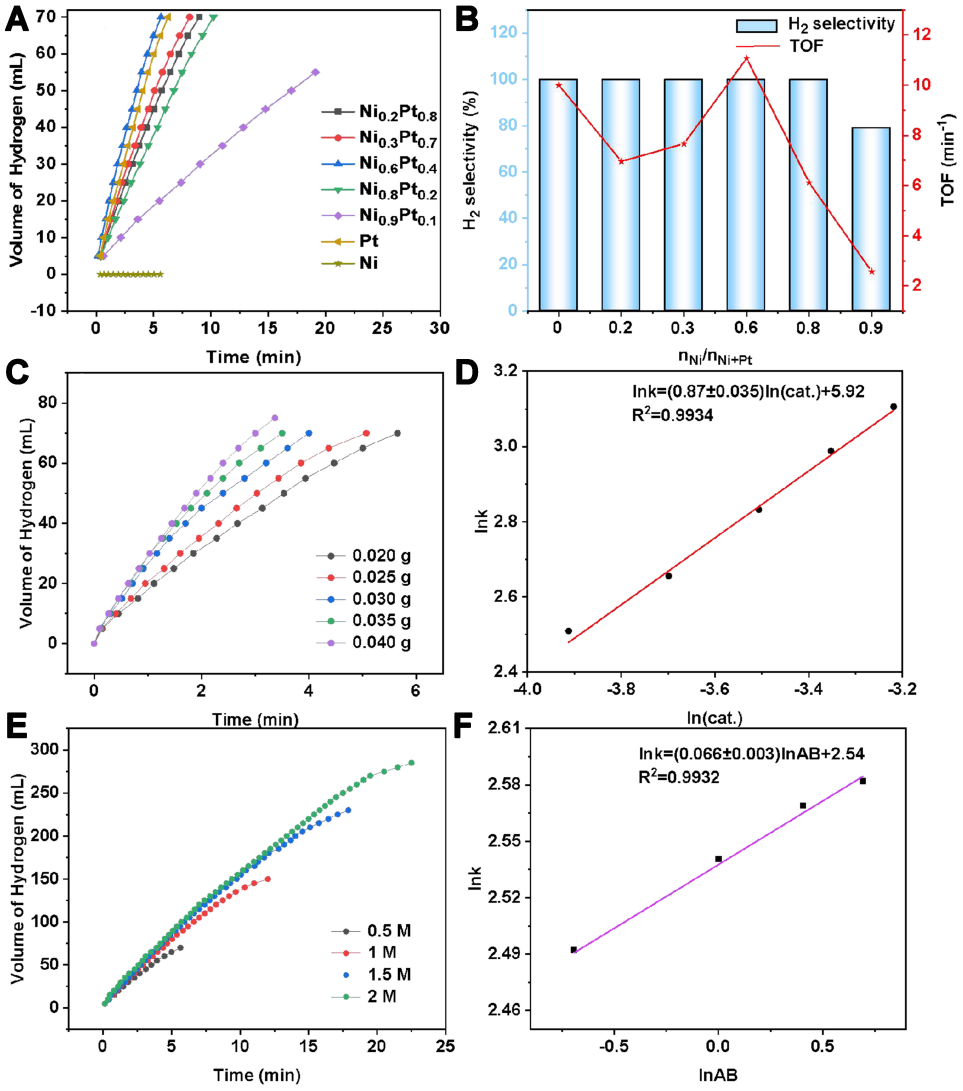

Figure 7. (A) Under 298 K conditions, the gas volume and reaction time curves of AB hydrolysis catalyzed by NiPt/CeMOF with different NiPt molar ratios; (B) TOF values corresponding to catalysts with different NiPt molar ratios; (C) Rate curves of AB hydrolysis catalyzed by $Ni_{0.6}Pt_{0.4}$/CeMOF catalysts with different dosages; (D) Relationship curve between logarithm of reaction rate and logarithm of catalyst dosage; (E) Relationship between AB hydrolysis reaction rate and concentration; (F) Relationship curve between logarithm of reaction rate and logarithm of concentration corresponding to different concentrations of AB. AB: Ammonia borane; CeMOF: cerium-based metal-organic framework; TOF: turnover frequency.

use. Kinetic studies indicate that the hydrogen generation reaction for AB hydrolysis is zero-order with respect to AB concentration, but first-order with respect to the catalyst amount. The outstanding performance of the NiPt/CeMOF catalyst is attributed not only to the unique structure of CeMOF but also to the strong interaction between NiPt alloy NPs and the CeMOF support, as confirmed by the aforementioned characterization techniques. This work not only provides a novel catalyst for efficient AB hydrolysis but also offers insights into the design of bimetallic catalysts supported on CeMOF, paving the way for more sustainable hydrogen production technologies.

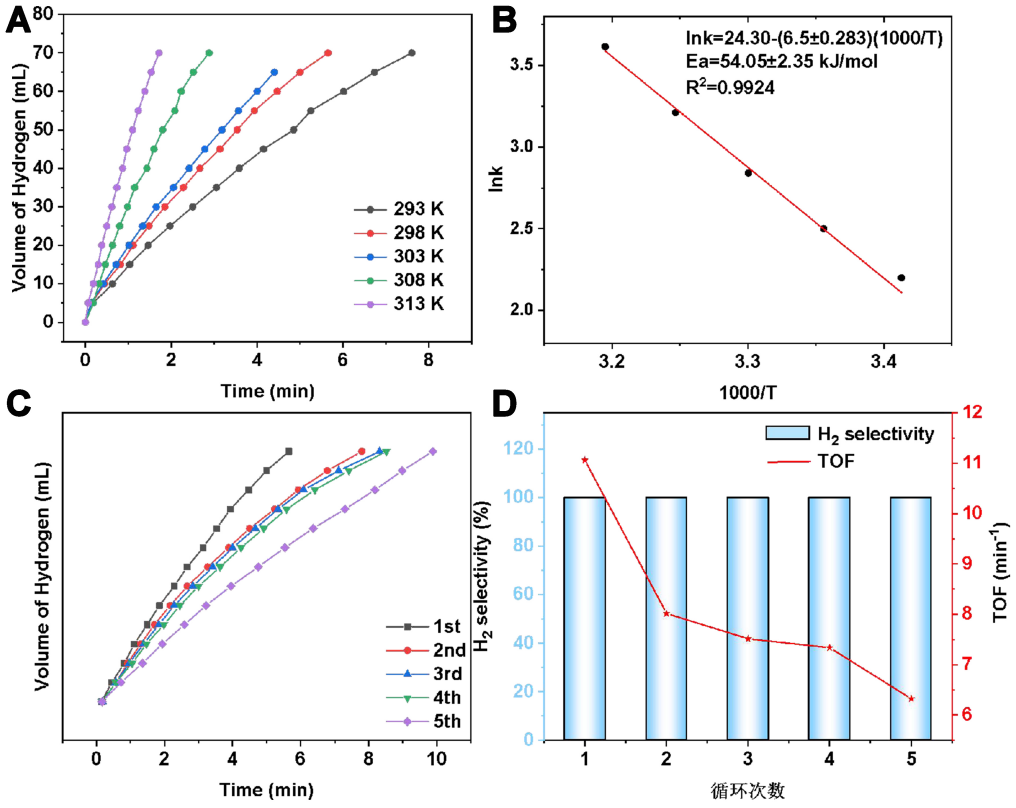

Figure 8. (A) Rate curves of AB hydrolysis catalyzed by $Ni_{0.6}Pt_{0.4}$/CeMOF at different temperatures; (B) Relationship curve between logarithm of reaction rate K and reciprocal of temperature; (C) Stable performance of $Ni_{0.6}Pt_{0.4}$/CeMOF (20 mg) catalyzing AB (0.5 M, 2 mL) hydrolysis cycle under 298 K conditions; (D) The TOF value corresponding to each cycle reaction of the catalyst. AB: Ammonia borane; CeMOF: cerium-based metal-organic framework; TOF: turnover frequency.

DECLARATIONS

Authors' contributions

Made substantial contributions to the conception and design of the study, performed data analysis and interpretation, and wrote original draft: Chen, X.; Hao, S.

Conducted the investigation of the study and data acquisition: Wang, J.; Xu, L.; Li, S.

Revised the manuscript and provided administrative, technical, and material support: Wang, J.; Wan, C.; Postnikov, P. S.

Availability of data and materials

The data that support the findings of this study are available from the corresponding author upon reasonable request.

Financial support and sponsorship

This work was supported by the National Natural Science Foundation of China (Nos. 22478001, 22108002 and 22108238), Excellent Youth Scholars Program of Higher Education Institutions of Anhui Province (2024AH030008), Excellent Young Scholars Program of Natural Science Foundation of Anhui Province (2408085Y005), and the Outstanding Scientific Research and Innovation Team Program of Higher Education Institutions of Anhui Province (No. 2023AH010015). The authors also express their gratitude to the Shiyanjia Lab (https://www.shiyanjia.com) for characterizing the materials used in this study.

Conflicts of interest

All authors declared that there are no conflicts of interest.

Ethical approval and consent to participate

Not applicable.

Consent for publication

Not applicable.

Copyright

REFERENCES

1. Truong-Phuoc, L.; Essyed, A.; Pham, X.; et al. Catalytic methane decomposition process on carbon-based catalyst under contactless induction heating. *Chem. Synth.* **2024**, *4*, 56. DOI
2. Fan, M.; Guo, J.; Fang, G.; et al. Microwave-pulse assisted synthesis of tunable ternary-doped 2D molybdenum carbide for efficient hydrogen evolution. *Chem. Synth.* **2024**, *4*, 36. DOI
3. Sun, Z.; Zhao, H.; Yu, X.; Hu, J.; Chen, Z. Glucose photorefinery for sustainable hydrogen and value-added chemicals coproduction. *Chem. Synth.* **2024**, *4*, 4. DOI
4. Graham, T. W.; Tsang, C. W.; Chen, X.; et al. Catalytic solvolysis of ammonia borane. *Angew. Chem. Int. Ed. Engl.* **2010**, *49*, 8708-11. DOI
5. Cao, C. Y.; Chen, C. Q.; Li, W.; Song, W. G.; Cai, W. Nanoporous nickel spheres as highly active catalyst for hydrogen generation from ammonia borane. *ChemSusChem* **2010**, *3*, 1241-4. DOI PubMed
6. Kong, J.; Li, R.; Liu, Y.; Xu, L.; Ye, M.; Wan, C. Research progress of hydrogen production from hydrous hydrazine decomposition catalyzed by metal catalysts. *Chin. J. Rare. Metals.* **2024**, *48*, 1177-90. DOI
7. Akbayrak, S.; Tonbul, Y.; Özkar, S. Tungsten(VI) oxide supported rhodium nanoparticles: highly active catalysts in hydrogen generation from ammonia borane. *Int. J. Hydrog. Energy.* **2021**, *46*, 14259-69. DOI
8. Wan, C.; Li, G.; Wang, J.; et al. Modulating electronic metal-support interactions to boost visible-light-driven hydrolysis of ammonia borane: nickel-platinum nanoparticles supported on phosphorus-doped titania. *Angew. Chem. Int. Ed. Engl.* **2023**, *62*, e202305371. DOI PubMed
9. Zheng, J.; Liang, Y.; Li, G.; et al. Mn-modified graphitic carbon nitride-supported bimetallic PtNi nanoparticles for hydrogen generation from hydrous hydrazine. *ChemistrySelect* **2022**, *7*, e202202690. DOI
10. Wen, M.; Wu, Q.; Peng, J.; Wu, Q.; Wang, C. Fabrication of Pt-loaded NiCo nanochains with superior catalytic dehydrogenation activity. *J. Colloid. Interface. Sci.* **2014**, *416*, 220-6. DOI
11. Zhang, H.; Gu, X.; Liu, P.; Song, J.; Cheng, J.; Su, H. Highly efficient visible-light-driven catalytic hydrogen evolution from ammonia borane using non-precious metal nanoparticles supported by graphitic carbon nitride. *J. Mater. Chem. A.* **2017**, *5*, 2288-96. DOI
12. Zhuo, Q.; Zhang, Y.; Du, Q.; Yan, C. Facile reduction of graphene oxide at room temperature by ammonia borane via salting out effect. *J. Colloid. Interface. Sci.* **2015**, *457*, 243-7. DOI
13. Langmi, H. W.; Mcgrady, G. S. Non-hydride systems of the main group elements as hydrogen storage materials. *Coord. Chem. Rev.* **2007**, *251*, 925-35. DOI
14. Wang, X.; Liao, J.; Li, H.; Wang, H.; Wang, R. Solid-state-reaction synthesis of cotton-like CoB alloy at room temperature as a catalyst for hydrogen generation. *J. Colloid. Interface. Sci.* **2016**, *475*, 149-53. DOI
15. Wan, C.; Liu, X.; Wang, J.; Chen, F.; Cheng, D. Heterostructuring 2D Co_2P nanosheets with 0D CoP via a salt-assisted strategy for boosting hydrogen evolution from ammonia borane hydrolysis. *Nano. Res.* **2023**, *16*, 6260-9. DOI
16. Wan, C.; Liang, Y.; Zhou, L.; et al. Integration of morphology and electronic structure modulation on cobalt phosphide nanosheets to boost photocatalytic hydrogen evolution from ammonia borane hydrolysis. *Green. Energy. Environ.* **2024**, *9*, 333-43. DOI
17. Li, G.; Li, R.; Liu, Y.; Xu, L.; Ye, M.; Wan, C. Preparation of Rh/N-SBC nanocatalyst and its catalytic performance for hydrolytic dehydrogenation of ammonia borane. *Chin. J. Rare. Metals.* **2024**, *48*, 944-54. DOI
18. Li, Z.; He, T.; Matsumura, D.; et al. Atomically dispersed Pt on the surface of Ni particles: synthesis and catalytic function in hydrogen generation from aqueous ammonia–borane. *ACS. Catal.* **2017**, *7*, 6762-9. DOI
19. Zhang, J.; Zheng, X.; Yu, W.; Feng, X.; Qin, Y. Unravelling the synergy in platinum-nickel bimetal catalysts designed by atomic layer deposition for efficient hydrolytic dehydrogenation of ammonia borane. *Appl. Catal. B. Environ.* **2022**, *306*, 121116. DOI
20. Zhou, S.; Yang, Y.; Yin, P.; Ren, Z.; Wang, L.; Wei, M. Metal-support synergistic catalysis in Pt/MoO_{3-x} nanorods toward ammonia borane hydrolysis with efficient hydrogen generation. *ACS. Appl. Mater. Interfaces.* **2022**, *14*, 5275-86. DOI PubMed
21. Huang, X.; Liu, Y.; Wen, H.; et al. Ensemble-boosting effect of Ru-Cu alloy on catalytic activity towards hydrogen evolution in ammonia borane hydrolysis. *Appl. Catal. B. Environ.* **2021**, *287*, 119960. DOI

22. Feng, Y.; Zhou, X.; Yang, J.; et al. Encapsulation of ammonia borane in Pd/halloysite nanotubes for efficient thermal dehydrogenation. *ACS. Sustain. Chem. Eng.* **2020**, *8*, 2122-9. DOI
23. Wan, C.; Zhou, L.; Xu, S.; et al. Defect engineered mesoporous graphitic carbon nitride modified with AgPd nanoparticles for enhanced photocatalytic hydrogen evolution from formic acid. *Chem. Eng. J.* **2022**, *429*, 132388. DOI
24. Wan, C.; Zhou, L.; Sun, L.; et al. Boosting visible-light-driven hydrogen evolution from formic acid over AgPd/2D g-C_3N_4 nanosheets Mott-Schottky photocatalyst. *Chem. Eng. J.* **2020**, *396*, 125229. DOI
25. Duan, H.; Hao, Q.; Xu, C. Nanoporous PtFe alloys as highly active and durable electrocatalysts for oxygen reduction reaction. *J. Power. Sources.* **2014**, *269*, 589-96. DOI
26. Dai, H.; Gao, L.; Liang, Y.; Kang, X.; Wang, P. Promoted hydrogen generation from ammonia borane aqueous solution using cobalt–molybdenum–boron/nickel foam catalyst. *J. Power. Sources.* **2010**, *195*, 307-12. DOI
27. Wan, C.; Li, R.; Wang, J.; et al. Silica confinement for stable and magnetic Co-Cu alloy nanoparticles in nitrogen-doped carbon for enhanced hydrogen evolution. *Angew. Chem. Int. Ed. Engl.* **2024**, *63*, e202404505. DOI
28. Li, M.; Hu, J.; Chen, Z.; Lu, H. A high-performance Pt–Co bimetallic catalyst with polyethyleneimine decorated graphene oxide as support for hydrolysis of ammonia borane. *RSC. Adv.* **2014**, *4*, 41152-8. DOI
29. Wang, S.; Zhang, D.; Ma, Y.; et al. Aqueous solution synthesis of Pt-M (M = Fe, Co, Ni) bimetallic nanoparticles and their catalysis for the hydrolytic dehydrogenation of ammonia borane. *ACS. Appl. Mater. Interfaces.* **2014**, *6*, 12429-35. DOI PubMed
30. Mori, K.; Miyawaki, K.; Yamashita, H. Ru and Ru–Ni nanoparticles on TiO_2 support as extremely active catalysts for hydrogen production from ammonia–borane. *ACS. Catal.* **2016**, *6*, 3128-35. DOI
31. Singh, A. K.; Xu, Q. Synergistic catalysis over bimetallic alloy nanoparticles. *ChemCatChem* **2013**, *5*, 652-76. DOI
32. Ge, Y.; Qin, X.; Li, A.; et al. Maximizing the synergistic effect of CoNi catalyst on α-MoC for robust hydrogen production. *J. Am. Chem. Soc.* **2021**, *143*, 628-33. DOI PubMed
33. Poon, P.; Wang, Y.; Li, W.; et al. Synergistic effect of Co catalysts with atomically dispersed CoN_x active sites on ammonia borane hydrolysis for hydrogen generation. *J. Mater. Chem. A.* **2022**, *10*, 5580-92. DOI
34. Dong, C.; Gao, Z.; Li, Y.; et al. Fully exposed palladium cluster catalysts enable hydrogen production from nitrogen heterocycles. *Nat. Catal.* **2022**, *5*, 485-93. DOI
35. Jeong, H.; Kwon, O.; Kim, B.; et al. Highly durable metal ensemble catalysts with full dispersion for automotive applications beyond single-atom catalysts. *Nat. Catal.* **2020**, *3*, 368-75. DOI
36. Yang, J.; Yuan, Q.; Liu, Y.; et al. Low-cost ternary Ni–Fe–P catalysts supported on Ni foam for hydrolysis of ammonia borane. *Inorg. Chem. Front.* **2019**, *6*, 1189-94. DOI
37. Wan, C.; Sun, L.; Xu, L.; et al. Novel NiPt alloy nanoparticle decorated 2D layered g-C_3N_4 nanosheets: a highly efficient catalyst for hydrogen generation from hydrous hydrazine. *J. Mater. Chem. A.* **2019**, *7*, 8798-804. DOI
38. Ren, W.; Liu, S.; Wang, Y.; et al. Sea urchin-like NiPt/$TiCeO_2$ catalyst for rapid and efficient hydrogen production from hydrous hydrazine. *J. Rare. Earths.* **2025**, *In Press*. DOI
39. Zhang, M.; Liu, L.; Lu, S.; Xu, L.; An, Y.; Wan, C. Facile fabrication of NiPt/CNTs as an efficient catalyst for hydrogen production from hydrous hydrazine. *ChemistrySelect* **2019**, *4*, 10494-500. DOI
40. Tomishige, K.; Kanazawa, S.; Ito, S.; Kunimori, K. Catalyst development for direct heat supply from combustion to reforming in methane reforming with CO_2 and O_2. *Appl. Catal. A. Gen.* **2003**, *244*, 71-82. DOI
41. Tomishige, K.; Kanazawa, S.; Sato, M.; Ikushima, K.; Kunimori, K. Catalyst design of Pt-modified Ni/Al_2O_3 catalyst with flat temperature profile in methane reforming with CO_2 and O_2. *Catal. Lett.* **2002**, *84*, 69-74. DOI
42. Du, Y.; Wang, B.; Kang, K.; et al. Signal synergistic amplification strategy based on functionalized CeMOFs for highly sensitive electrochemical detection of phenolic isomers. *Microchem. J.* **2022**, *177*, 107285. DOI
43. Chen, X.; Lin, Y.; Li, W.; et al. Amidoximated CeMOFs superstructures with algae-removing properties for efficient uranium extraction from simulated seawater. *Sustain. Mater. Technol.* **2022**, *34*, e00521. DOI
44. Li, Z.; Ma, C.; Qi, M.; et al. CeO_2 from pyrolysis of MOFs for efficient catalytic combustion of VOCs. *Mol. Catal.* **2023**, *535*, 112857. DOI
45. Dai, S.; Montero-Lanzuela, E.; Tissot, A.; et al. Room temperature design of Ce(IV)-MOFs: from photocatalytic HER and OER to overall water splitting under simulated sunlight irradiation. *Chem. Sci.* **2023**, *14*, 3451-61. DOI PubMed PMC